

Article

Design of a Hand-Launched Solar-Powered Unmanned Aerial Vehicle (UAV) System for Plateau

Xin Zhao ¹, Zhou Zhou ^{1,*}, Xiaoping Zhu ² and An Guo ¹

¹ School of Aeronautics, Northwestern Polytechnical University, Xi'an 710072, China; xin_zhao@mail.nwpu.edu.cn (X.Z.); guoanuav@mail.nwpu.edu.cn (A.G.)

² Science and Technology on UAV Laboratory, Northwestern Polytechnical University, Xi'an 710072, China; zhuxp@nwpu.edu.cn

* Correspondence: zhouzhou@nwpu.edu.cn

Received: 8 January 2020; Accepted: 7 February 2020; Published: 14 February 2020



Abstract: This paper describes our work on a small, hand-launched, solar-powered unmanned aerial vehicle (UAV) suitable for low temperatures and high altitudes, which has the perpetual flight potential for conservation missions for rare animals in the plateau area in winter. Firstly, the conceptual design method of a small, solar-powered UAV based on energy balance is proposed, which is suitable for flight in high-altitude and low-temperature area. The solar irradiance model, which can reflect the geographical location and time, was used. Based on the low-temperature discharge test of the battery, a battery weight model considering the influence of low temperature on the battery performance was proposed. Secondly, this paper introduces the detailed design of solar UAV for plateau area, including layout design, structure design, load, and avionics. To increase the proportion of solar cells covered, the ailerons were removed and a rudder was used to control both roll and yaw. Then, the dynamics model of an aileron-free layout UAV was developed, and the differences in maneuverability and stability of aileron-free UAV in plateau and plain areas were analyzed. The control law and trajectory tracking control law were designed for the aileron-free UAV. Finally, the flight test was conducted in Qiangtang, Tibet, at an altitude of 4500 m, China's first solar-powered UAV to take off and land above 4500 m on the plateau in winter (−30 °C). The test data showed the success of the scheme, validated the conceptual design method and the success of the control system for aileron-free UAV, and analyzed the feasibility of perpetual flight carrying different loads according to the flight energy consumption data.

Keywords: solar-powered UAV; perpetual flight; conceptual design; aileron-free; flight control system; flight test

1. Introduction

With the development of the world economy, energy crisis and environmental pollution are becoming a serious problem. In recent years, with the rapid improvement of technology of solar cell and secondary battery, solar-powered aircraft, due to the advantages of environmental protection and long endurance, following the 'Pathfinder' [1] and 'Helios' [2], the world set off a research upsurge of solar-powered UAV once again. Solar-powered UAV, which converts solar energy into electricity and stores it in secondary batteries during daytime flight, has better endurance than conventional aircraft and may even be able to fly permanently. The long-endurance capability of the solar-powered UAV platform is particularly important in rescue missions, forest fire prevention, communication coverage, and protection of endangered animals. In view of the extreme flight environment in the plateau region, this paper proposes a design method of small, solar-powered UAV suitable for low-temperature and high altitude areas, including a solar irradiance model that can reflect the geography and time and a

battery weight model that considers the impact of low temperature on battery performance. Based on this, a small aileron-free UAV was developed for ecological monitoring and animal protection in plateau areas. This paper also developed the dynamics model of aileron-free UAV, analyzed the characteristics of UAV's stability and maneuverability in high-altitude flight, and designed the control and tracking system for high-altitude flight. Finally, in Qiangtang, Tibet, China's first solar-powered UAV took off and landed at an altitude of more than 4500 m. The experiment verified the correctness of the design method and the control method, and analyzed the feasibility of the perpetual flight with different loads according to the flight energy consumption data (Figure 1).

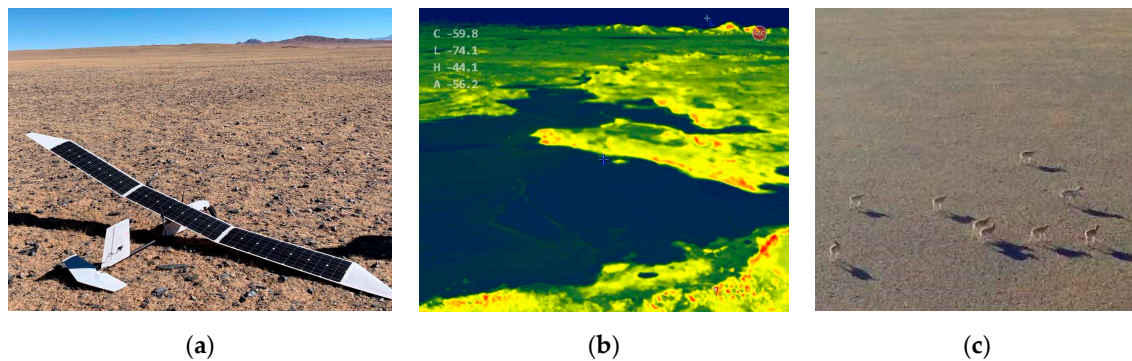


Figure 1. The solar-powered unmanned aerial vehicle (UAV) used for ecological monitoring and animal protection: (a) Mini-Phantom (MP) solar-powered UAV, (b) infrared pod for ecological monitoring, (c) Tibetan antelopes photographed by optical camera.

In recent years, solar-powered aircraft have been developed in both manned and unmanned aircraft. In terms of manned solar aircraft, 'Solar Impulse 2', the world's largest solar-powered airplane, successfully completed the world's first solar-powered flight around the world on 26 July 2016 [3]. On the other hand, many researchers focus on employing large-scale solar-powered high-altitude long-endurance (HALE) UAVs as atmospheric satellites. Typical examples are 'Solara' [4] and 'Zephyr S', the latter of which has broken the previous record of 14 days set by the 'Zephyr 7' prototype [5] with approximately 25 days and 23 h of flight on 11 July 2018 [6]. In contrast, smaller-scale, solar-powered UAVs are mostly designed for low-altitude long-endurance (LALE) applications. In 2008, 'sky sailor', a small solar-powered UAV from Switzerland, flew for 27 h. The structural design of the UAV referred to the glider for competition and it weighed only 780 g [7]. The 'AtlantikSolar' small UAV from the Swiss Federal Institute of Technology Zurich completed a flight of 81.5 h in July 2015, setting an endurance record for an aircraft under 50 kg. Compared with large solar-powered aircraft, small solar-powered UAV have higher structural weight coefficient and lower load capacity, so they are suited for low-altitude and long-endurance missions. Noth proposed a matching parameter model of energy and power for perpetual flight [7] of small solar UAV in 2008. Based on the energy system model, Philipp Oettershagen proposed an energy-robust design method that allows design of solar-powered UAVs for energetically robust perpetual flight in sub-optimal meteorological conditions [8]. In both methods, the solar irradiance model was a simplified sinusoidal model. Small solar-powered UAVs fly mostly at low altitudes, so most previous studies did not consider the effect of low temperatures on battery performance.

Section 2 presents the conceptual design method of perpetual flight suitable for flight on low temperature and high altitude based on energy balance, and explores the feasibility of perpetual flight of small hand-launched solar-powered UAV in plateaus such as Tibet, China, which is particularly important for the protection of rare animals such as the Tibetan antelope. In this paper, irradiance predicted model [9] was adopted to establish the solar energy model, which can more accurately reflect the solar irradiance at different geographical locations and time. The accuracy of the irradiance model was verified by experimental data, which were measured by the total solar irradiance meter. In this

part, the low-temperature discharge test was carried out to test the influence of low temperature on the battery discharge performance, and the battery weight model considering the influence of low temperature was proposed.

Section 3 presents the detailed design of the Mini-Phantom (MP) solar UAV. The MP UAV system design includes layout design, structure design, payloads, and avionics selection.

Sections 4 and 5 presents the dynamic model and control algorithms, in which the model of the high-altitude propulsion system was modified through the low-altitude dynamic experiment. Based on the motion equation of UAV, this section analyzes the change of flight quality with altitude and velocity when flying in plateaus and plain areas. In addition, longitudinal height and lateral trajectory tracking controllers were designed based on successive loop closure for plateau flight environment. Flight tests were conducted on the Tibetan plateau. Experimental results verified the correctness of the design method and control algorithm, and analyzed the feasibility of permanent flight in the plateau.

Section 6 contributes an outlook into the specific condition and the whole process is summarized.

2. Conceptual Design Method

To achieve perpetual flight, the solar-powered UAV was designed based on weight balance and energy balance. The former determined whether the plane would fly as expected. In the latter, the balance between the energy collected by the solar cells and the energy consumed in the flight determined the endurance of the UAV. In order to simplify the model, UAV's cruise state was steady level flight at the same altitude. During the cruise, there was no energy conversion through climbing and descending.

In design, the first consideration was the balance of forces. Similar to conventional long-endurance aircraft, solar-powered UAV have a single flight state, which is a 'single design point' flight platform. The balance between lift and weight and the balance between thrust and drag are necessary during steady flight.

Power balance is also important in the design of solar-powered aircraft. In order to achieve the goal of perpetual flight, the total energy collected by the solar cells during the day flight must be more than the energy consumed during the flight. Besides, the remaining energy from the batteries should be sufficient for the night flight at the end of the day.

In this paper, the analytical and continuous approximation method was used, that is, the model describing the characteristics of each part was used to establish the relationship between each part model by analytic equation. The advantage of this method is that the analytical solution can be obtained directly and the unique optimal design can be obtained directly. However, the method needs accurate mathematical models.

In this paper, first of all, the power expression of the plane in cruise was established, and then the total energy collected by the solar cells during the day flight was obtained based on the solar irradiance model. Then, the weight prediction model of each part of the aircraft was given, and a closed loop was formed according to the relationship between the energy, so as to obtain the analytical solution that makes the scheme feasible.

2.1. Power of Level Flight

The lift and drag of the aircraft can be obtained from Formula (1), where C_L and represent C_D the lift and drag coefficients, respectively. ρ is air density and S is wing area. According to these two basic formulas, the mechanical power consumed during cruise can be obtained, as shown in Formula (2).

$$\begin{cases} W = L = \frac{\rho}{2} V^2 S C_L \\ T = D = \frac{\rho}{2} V^2 S C_D \end{cases} \quad (1)$$

$$P_{lev} = TV = \frac{mg}{(L/D)} V = \frac{C_D}{C_L^{3/2}} \sqrt{\frac{2ARg^3}{\rho}} \frac{m^{3/2}}{b} \quad (2)$$

The total electrical power of the aircraft during cruise P_{elec_tot} included mechanical power and electrical power. The efficiency of the motors η_{mot} , electronic controllers η_{ctrl} , and propellers η_{plr} , as well as the power consumption of avionics P_{av} and payload instrument P_{pld} must be considered. Since the battery voltage was higher than the voltage of avionics and payload instrument, the efficiency of step-down η_{bec} , also called battery elimination circuit (BEC), should also be considered. In order to improve the reliability and maintainability, MP UAV's propulsion system was propeller-motor direct drive. The efficiency of gearbox can be ignored. The total electrical power during cruise is shown in Formula (3).

$$P_{elec_tot} = \frac{1}{\eta_{ctrl}\eta_{mot}\eta_{plr}}P_{lev} + \frac{1}{\eta_{bec}}(P_{av} + P_{pld}) \quad (3)$$

The total energy consumed during the all-day flight is shown in the Formula (4). Unlike daytime flight, all energy consumed during the night flight was from the battery, so the charging efficiency η_{chrg} and η_{dchrg} discharging efficiency of battery also need to be considered.

$$E_{elec_tot} = P_{elec_tot} \left(T_{day} + \frac{T_{night}}{\eta_{chrg}\eta_{dchrg}k_{temp}} \right) \quad (4)$$

where T_{day} and T_{night} present day time and night time respectively, and k_{temp} presents the temperature influence factor. At dusk and dawn, when the solar energy collected by solar cells is less than the required power, the energy comes from both the solar cells and battery, and the conversion from one source to another is gradual. The process of energy source conversion is seen as instantaneous to simplify the calculation.

2.2. Solar Energy Obtained during the Day

In this paper, solar irradiance predicted model was used to estimate the solar irradiance. The solar energy obtained throughout the day can be calculated by solar irradiance model. Irradiance depends on many variables, such as geographical location, time, plane orientation, weather conditions, and albedo, which represents the reflection of ground [10]. In general, the total irradiance I_{tot} consists of direct irradiance I_b and scattering irradiance I_d . The direct irradiance [10] is shown in Formula (5).

$$\begin{cases} I = I_0 \exp \left(- \frac{c_s \exp(-\frac{h}{s_s})}{\left[\sin \left(\frac{\alpha_s + \alpha_{dep}}{1 + \alpha_{dep}/90} \right) \right]^{s_s + \frac{h}{h_p}}} \right) \\ I_0 = G_{sc} [1 + 0.033 \cos(360n_d/365)] \\ \alpha_{dep} = 0.57 + \arccos(R_{eth}/(R_{eth} + h)) \end{cases} \quad (5)$$

where G_{sc} is the standard solar radiation constant, taking 1367 W/m^2 . I_0 is the solar irradiance outside the atmosphere on the n_d day of the year, c_s and s_s are both constants, taking 0.357 and 0.678, respectively. The h is the flight altitude of solar aircraft and α_{dep} is the modified value relative to ground. R_{eth} is the radius of the Earth. The α_s is determined by local latitude φ_{lat} , solar declination angle δ_s , and solar hour angle θ_h . The relationship is shown in Formula (6).

$$\begin{cases} \sin \alpha_s = \sin \varphi_{lat} \sin \delta_s + \cos \varphi_{lat} \cos \delta_s \cos \theta_h \\ \delta_s = 23.45 \sin \left(360 \frac{n_d + 284}{365} \right) \end{cases} \quad (6)$$

in which the corresponding relationship between solar hour angle θ_h and solar hour H_s is shown in Formula (7).

$$\theta_h = 15(H_s - 12) \quad (7)$$

Solar time in any region can be calculated by Formula (8).

$$\begin{cases} H_s = H_{ct} + \frac{L_{st}-L_{ct}}{15} + \frac{E_t}{60} \\ E_t = 0.0172 + 4.28 \cos B - 7.35 \sin B - 3.35 \cos 2B - 9.732 \sin 2B \\ B = \frac{360}{365}(n_d - 1) \end{cases} \quad (8)$$

where H_{ct} is the local time. L_{st} is the standard longitude adopted by H_{ct} . L_{ct} is the local longitude. E_t is the correction between H_s and H_{ct} caused by the revolution of earth. It is assumed that the scattering irradiance is omnidirectional and linearly proportional to the direct irradiance. Here, the proportionality coefficient is 0.08 [9]. The relationship between scattering irradiance and direct irradiance is shown in Formula (9).

$$I_d = 0.08I_b \exp\left(-\frac{h}{h_s}\right) \quad (9)$$

The total solar irradiance considering latitude, altitude, and flight time is expressed as Formula (10).

$$I_{tot} = I_b \sin \alpha_s + I_d \quad (10)$$

The solar irradiance of Xi'an, China, on 27 May 2017 at an altitude of 400 m, simulated by the irradiance prediction model, is shown in the Figure 2a. The measured data in the figure was measured on 27 May 2017. For the parameters, such as the maximum irradiance, the corresponding time, and the time of the sun setting, the irradiance model fit well with the measured data. Figure 2b presents the measuring instruments of solar irradiance.

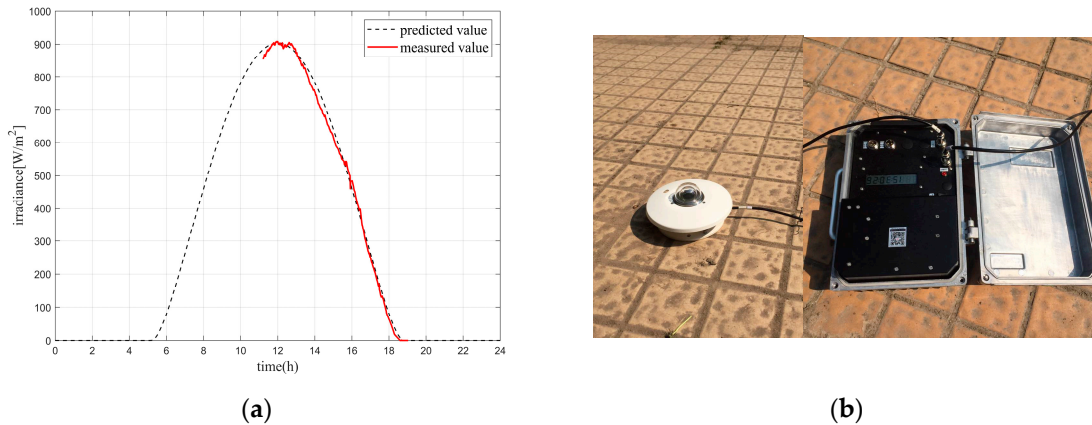


Figure 2. (a) Comparison of predicted and measured values of solar irradiance on 27 May 2017, Xi'an, China (34°16' N 108°54' E). (b) Measuring instrument of solar irradiance.

Obviously, energy density captured by solar cells is the integral of irradiance with respect to time, in which energy density is the ratio of captured energy to solar cell area. Considering the actual laying area of solar cells A_{sc} , packaging efficiency η_{cbr} , electrical energy conversion efficiency η_{sc} , maximum power point tracker (MPPT) efficiency η_{mppt} , and weather influence factor, the solar energy captured by solar cells of the aircraft is shown in Formula (11).

$$E_{sun_tot} = \int I_{tot}(t)dt A_{sc} \eta_{wthr} \eta_{sc} \eta_{cbr} \eta_{mppt} \quad (11)$$

2.3. Weight Estimation Model

The total takeoff weight of an aircraft consists of the weight of components, which directly affects the flight power. In order to calculate the flight power accurately, the weight estimation model should be precise as much as possible. The weight of the main components of the UAV includes weight of

mission payloads m_{pld} and avionics m_{av} , structural weight m_{af} , weight of solar cells m_{sc} , weight of MPPT m_{mppt} , weight of batteries m_{bat} , and weight of propulsion system m_{prop} . Payload and avionics are fixed weights, which are related to mission requirements and shown in Formula (12). The weight of other components is related to the parameters of UAV size, flight power, etc.

$$m_{fixed} = m_{av} + m_{pld} \tag{12}$$

The weight of aircraft structures is difficult to model accurately. Most structural weight estimation models are empirical formulas, which are based on a large amount of data from existing aircraft. Romeo [11], Youngblood [12], and Rizzo [13] proposed several weight estimation models for large wingspan, solar-powered aircraft, which used wing area and wingspan as variables to estimate the structural weight of the aircraft. Noth [7] screened the data by wingload and structure weight to modify the parameters of the weight estimation model, which can apply to the small, light-structure, solar-powered UAV (Formula (13)).

$$m_{af} = k_{af}AR^{x_2}b^{x_1} \tag{13}$$

The power captured by the solar cells is linear with the laid area. The area of the solar cells determines whether the energy captured from sun is enough to balance the energy consumed in flight. The area and weight of solar cells can be calculated based on the energy–power balance, which is shown in Formula (14).

$$\begin{cases} A_{sc} = \frac{1}{\eta_{sc}\eta_{cbr}\eta_{mppt}\eta_{wthr}} \int I_{tot} \left(T_{day} + \frac{T_{night}}{\eta_{charg}\eta_{dcharg}k_{temp}} \right) P_{elec_tot} \\ m_{sc} = A_{sc}(k_{sc} + k_{enc}) \end{cases} \tag{14}$$

where k_{sc} presents the surface density of solar cells. However, exposed solar cells, which are fragile and oxidizing, need to be encapsulated for practical use. Surface density of packaging k_{enc} also needs to be considered.

MPPT is used to track the maximum power by adjusting the voltage of the solar cells, and its weight is proportional to the maximum power, that is, proportional to the area of the solar cells. The weight of MPPT is shown in Formula (15), where P_{solmax} presents the maximum input power of solar cells, obtained by measurement.

$$m_{mppt} = k_{mppt}P_{solmax} = k_{mppt}I_{max}\eta_{sc}\eta_{cbr}\eta_{mppt}A_{sc} \tag{15}$$

For batteries, their weight is proportional to the energy stored and inversely proportional to energy density k_{bat} , which is an important parameter to evaluate battery performance. However, the energy density of the battery is inversely proportional to the discharge power. For solar-powered aircraft that focus on cruise, the constraint of discharge power can be ignored. Therefore, high-energy density batteries, such as lithium-ion batteries, should be selected. For perpetual flight, the requirement of minimum battery weight is that the energy stored by batteries is sufficient for night flight, which is shown in Formula (16).

$$m_{bat} = \frac{T_{night}}{\eta_{dchrg}k_{bat}}P_{elec_tot} \tag{16}$$

Another factor that cannot be ignored that affects battery performance is ambient temperature. For the lithium-ion batteries concerned in this paper, generally speaking, the most suitable operating temperature is 0–40 °C. When the temperature is lower than 0 °C or higher than 40 °C, the battery discharge efficiency will decrease sharply, which means the reduction of battery capacity or the increase of battery weight required for aircraft parameters.

The flight environment of MP solar UAV was the plateau area in winter. In order to study the influence of low temperature on battery capacity, the low-temperature discharge test of energy system

was conducted in a low-temperature and low-pressure test chamber, experimental instruments are shown in Figure 3.



Figure 3. The discharge test of energy system in low-temperature and low-pressure test chamber.

The test subjects included propulsion systems (brushless motor, propeller, and motor controller), autopilot systems, and a lithium-ion battery rated at 230 Wh for low-temperature resistance. The test chamber provided a $-25\text{ }^{\circ}\text{C}$, 540 hPa low-temperature, and low-pressure simulation environment. During the test, the propulsion system operates with a constant throttle command until the voltage reached the battery’s protective voltage, and the sensor recorded the output power, voltage, and current of the battery bus. Figure 4 shows the test results of the low-temperature discharge test, which are the changes of power, voltage, and current with time, respectively.

In the test, the system worked normally under low-temperature conditions, the voltage fluctuation range was small, basically linear decline. The amplitude of current fluctuation was about 0.4 A and the smoothed current-time curve also presented a linear decline.

By integrating the power-time curve discretely, the total output energy of the battery in the test can be obtained, which was about 159.01 Wh. At a low temperature of $-25\text{ }^{\circ}\text{C}$, the discharge efficiency of the battery was about 69.1%. In the discharge experiment at room temperature ($20\text{ }^{\circ}\text{C}$), the output energy was about 220.73 Wh and the discharge efficiency of the battery was about 95.9%. Therefore, solar-powered UAV flying in extreme environments, temperature impact factor k_{temp} must be considered in the design process. In this test, the temperature influence factor was about 0.72. In order to prevent the low temperature from damaging the battery performance, the weight of the insulation material or the temperature control system of the battery also needs to be considered in the high-altitude, solar-powered UAV design. The battery weight model considering the effect of low temperature is shown in the Formula (17).

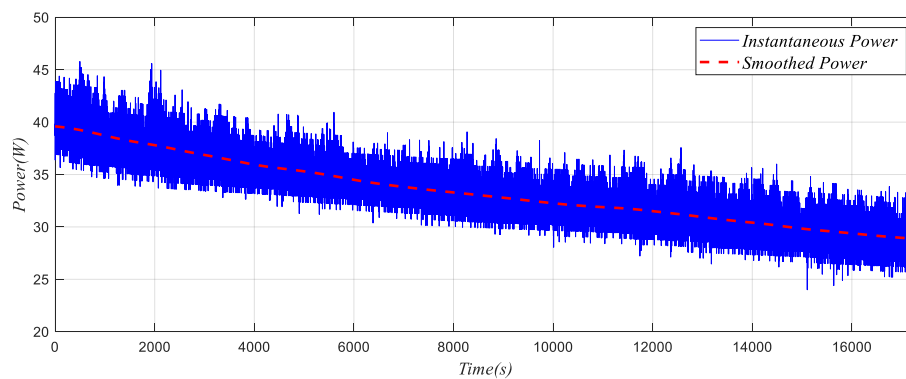
$$m_{bat} = \frac{T_{night}}{\eta_{dchrg} k_{bat} k_{temp}} P_{elec_tot} \tag{17}$$

Electric propulsion systems usually contain propellers, motors, controllers, gearbox, etc. For small, solar-powered UAVs, a gearbox is not necessary to reduce the system complexity and cost. In order to simplify the model, the propulsion system is considered as a whole, and the weight of the propulsion system is positively correlated with the maximum power. Factor k_{prop} is used to predict the

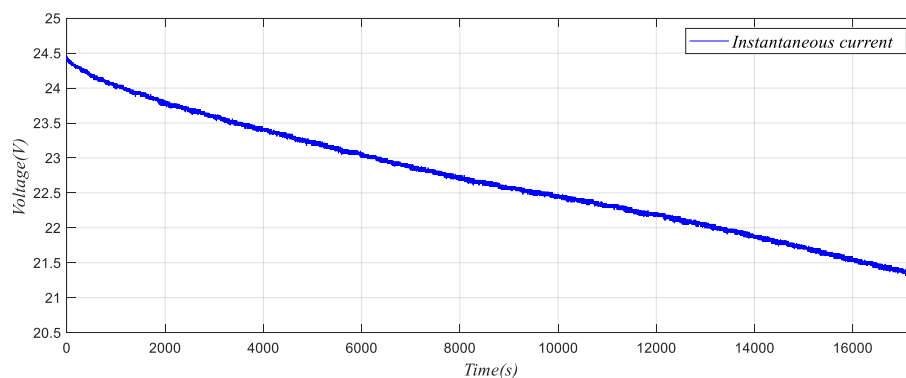
weight of the propulsion system, whose value is obtained by statistical data. The weight model of propulsion system is shown in Formula (18).

$$m_{prop} = k_{prop} P_{lev} = k_{prop} \frac{C_D}{C_L^{3/2}} \sqrt{\frac{2ARg^3}{\rho}} \frac{m^{3/2}}{b} \tag{18}$$

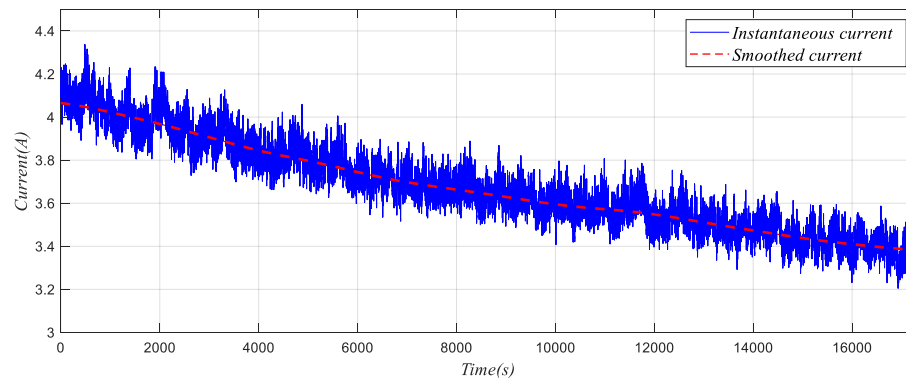
The total energy consumed during day and night flight can be obtained by the aerodynamic model and the weight model system. The closed loop of the energy balance is reconstructed by the weight model of each component. Figure 5 presents a detailed loop that visually represents the conceptual design process of the solar-powered UAV in this paper.



(a)



(b)



(c)

Figure 4. Test result of low-temperature discharge test at -25 degrees Celsius, 540 hPa: (a) Power, (b) voltage, (c) current.

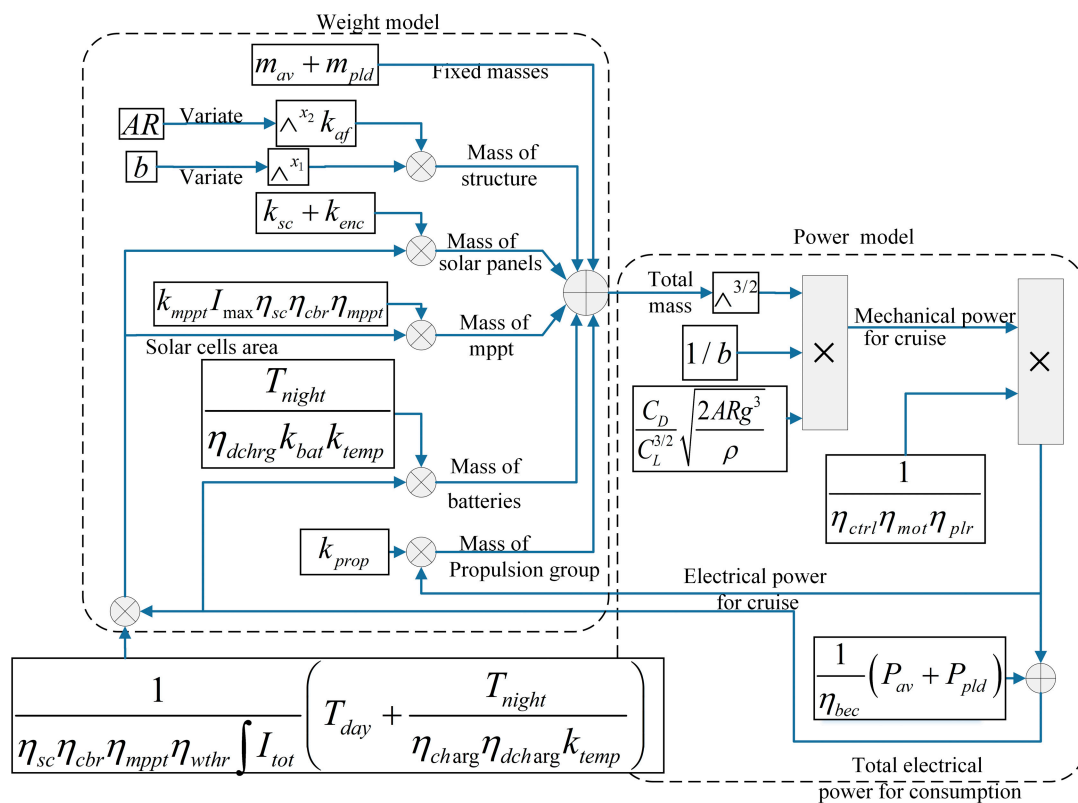


Figure 5. Conceptual design progress of solar-powered UAV based on energy balance.

The parameters contained in Figure 5 can be divided into three categories.

The first part is the weight prediction model, which consists of the weight models of each component. The parameters are mostly constant, representing the development level of products in various industries at the present stage. These constants, which are shown in Table 1, are partly fitted from statistics and partly from actual measurements.

Table 1. The values of parameters correspond to the Mini-Phantom UAV design.

Parameter	Value	Unit	Description
C_L	0.8	-	Lift coefficient
C_D	0.04	-	Drag coefficient
I_{max}	950	[W/m ²]	Maximum irradiance
k_{temp}	0.89	-	Temperature influence factor (5 °C)
k_{bat}	290	[Wh/kg]	Energy density of Li-ion battery
k_{sc}	0.29	[kg/m ²]	Mass density of solar cells
k_{enc}	0.13	[kg/m ²]	Mass density of encapsulation
k_{mppt}	0.0042	[kg/W]	Mass to power ratio of MPPT
k_{prop}	0.008	[kg/W]	Mass to power ratio of propulsion group
k_{af}	0.44/9.81	[kg/m ³]	Structural mass constant
m_{av}	0.11	[kg]	Mass of autopilot system
η_{bec}	0.8	-	Efficiency of step-down converter
η_{sc}	0.2	-	Efficiency of solar cells
η_{cbr}	0.9	-	Efficiency of the curved solar panels
η_{charg}	0.95	-	Efficiency of battery charge
η_{ctrl}	0.95	-	Efficiency of motor controller
η_{dcharg}	0.95	-	Efficiency of battery discharge
η_{mot}	0.9	-	Efficiency of motor
η_{mppt}	0.97	-	Efficiency of MPPT
η_{plr}	0.85	-	Efficiency of propeller
P_{av}	1.5	[W]	Power of autopilot system
x_1	3.1	-	Airframe mass wingspan exponent
x_2	-0.25	-	Airframe mass aspect ratio exponent

The second part is the aerodynamic model, including the parameters that reflect the flight environment and aircraft lift and drag characteristics, which are mainly determined by the flight mission objectives. Mission parameters of Mini-Phantom UAV are shown in Table 2. In the aerodynamic model, the aircraft layout parameters are represented by aspect ratio and wingspan as input variables.

Table 2. Mission parameters for Mini-Phantom UAV.

Parameter	Value	Unit	Description
m_{pld}	0.1	[kg]	Payload mass
η_{wthr}	0.85	-	Irradiance margin factor
P_{pld}	2	[W]	Payload power consumption
ρ	0.78	[kg/m ³]	Air density (4500 m)
T_{day}	14.3	[h]	Summer day duration (34.3° N)

The third part is the balance between the energy consumed by the aircraft and the solar energy captured, which connects the weight model with the aerodynamic model, forming a closed loop, through which the optimal aircraft layout can be obtained.

3. Detailed Design

3.1. Layout Design

Solar-powered UAVs adopt various forms of layout, such as flying-wing layout, tandem-wing layout, conventional layout, etc. Among them, the flying-wing layout solar-powered UAV is typically representative of NASA's 'Pathfinder' and 'Helios'.

Compared with the conventional layout, the wing layout has the advantages of light structure weight and high aerodynamic efficiency, which are crucial for long-endurance aircraft. However, the static stability of the flying-wing layout is usually weak, and it is more sensitive to the changes of flight altitude and speed. Moreover, the flight angle of attack of the flying-wing layout UAV is less robust, and the pitching moment is easy to diverge in the state of high angle of attack, which is usually solved by split-drag-rudder or differential thrust control. Therefore, the flying-wing layout is usually used for large wingspan solar UAVs, and the takeoff and landing should be carried out in good conditions.

The tandem wing layout consists of two wings, the front and rear, and has a higher lift coefficient with the same wingspan. When the aircraft is disturbed, the fuselage has good aeroelastic characteristics compared with the conventional layout. The stall characteristics of this layout are similar to those of the canard layout. In order to ensure good stall characteristics, the front wing stalls before the rear wing stalls, which has good longitudinal safety in flight. However, in the takeoff and landing stage, the rear wing cannot reach the maximum lift point, so good landing site conditions and long takeoff and landing distance are required.

The conventional layout facilitates the design of the fuselage and the arrangement of loads and equipment. Moreover, it has the advantages of high robustness and better stability at high angle of attack, and low takeoff and landing speed, which is especially suitable for small solar-powered UAVs with hand-launched takeoff and hard landing.

A fully functional prototype was built, named Mini-Phantom Solar (MP Solar). Considering the extreme flight environment (4600 m altitude, −30 °C temperature), the MP Solar UAV (Figure 6) is of a conventional configuration with an aileron-free rudder and an all-moving elevator. It is worth mentioning that the full-motion elevator is designed to facilitate disassembly and transportation, and during the landing phase, the full-moving elevator is deflected at a large degree so that the UAV enters a deep stall before it touches ground, which allows the aircraft to achieve a lower landing speed.

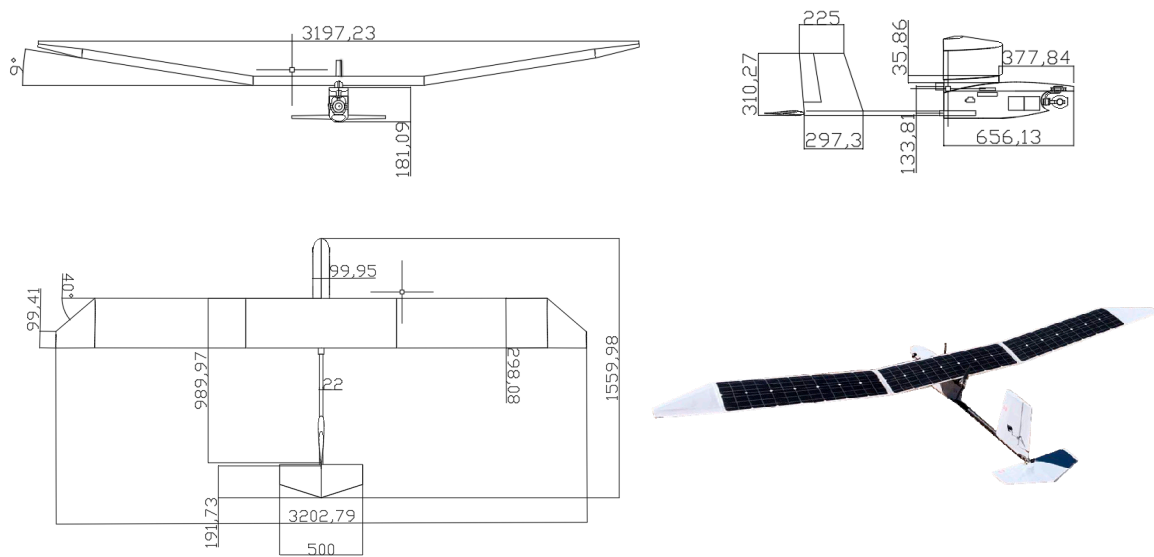


Figure 6. The Mini-Phantom Solar UAV. Dimensions are given in mm.

The main wing, with a 3.2 m wingspan, can be split into three segments of similar size to facilitate transport. The aileron-free design of the rectangular wing ensures the wing’s integrity, which increases the proportion of solar cells laid (14 units of solar cells laid as two rows on each wing segment). The outer wing has a dihedral angle of 9 degrees to improve the lateral stability of the aircraft. The layout characteristics are summarized in Table 3.

Table 3. Design characteristics of Mini-Phantom Solar UAV.

Parameter	Value	Unit	Description
AR	10.6	-	Aspect ratio
b	3.2	m	Wingspan
S_{win}	0.934	m ²	Wing area
S_{ele}	0.06	m ²	Horizontal tail area
S_{vert}	0.08	m ²	Vertical tail area
S_{rud}	0.017	m ²	Rudder area
V_H	0.21	-	Horizontal tail volume
V_V	0.28	-	Vertical tail volume
m	2.9	kg	Total mass
m_{bat}	1.2	kg	Battery mass
m_{Mpld}	0.6	kg	Max payload mass
V	10	m/s	Flight speed

3.2. Aerodynamic Design

The lift–drag ratio of an aircraft is used to evaluate the aerodynamic efficiency and is the key parameter affecting the endurance of solar-powered UAV. The flying-wing layout has a high lift–drag ratio due to the absence of fuselage and tail. In order to improve aerodynamic efficiency, the layout of flying-wings is used for reference in aerodynamic design. The airfoil of the main wing is optimized on the basis of the low Reynolds number laminar airfoil to make its tail have the characteristics of reverse camber (Figure 7b), reduce the nose-down pitching moment generated by the main wing, and thus reduce the requirement for the horizontal tail volume (Tables 1 and 3). The airfoil of tails is NACA0009, which is developed by National Advisory Committee for Aeronautics (NACA).

The aerodynamic efficiency of the UAV can be improved by increasing the reverse camber of airfoil, reducing the area of the horizontal tail and the length of the rear fuselage, and the stability of the UAV at high angle of attack can be guaranteed by the existence of the tail.

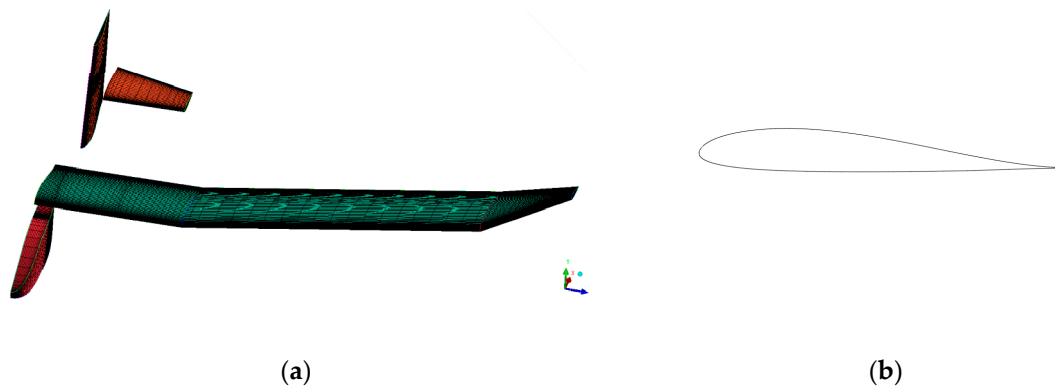


Figure 7. (a) Aerodynamic computing grid model. (b) Optimized airfoil of main wing.

Aerodynamic calculations were carried out for the shape of the UAV, among which the turbulence model was the Spalart–Allmaras model, and the calculated state was: Flight altitude was 5000 m, speed was 10.5 m/s.

Figure 8 shows the change of aerodynamic parameters of the aircraft with the angle of attack. When the UAV cruised at an altitude of 5000 m at a speed of 10.5 m/s, the maximum lift-to-drag ratio was 18.4, which was obtained at 2 degrees of angle of attack, which was consistent with the UAV’s trim angle of attack. At the trim angle of attack, the lift coefficient of the UAV was about 0.8 and the stall angle of attack was about 9 degrees.

It can be seen from the pitching moment curve that the pitching moment converged in the whole process and maintained a good linear relationship. The static stability margin was about 13.8% near the cruising point. With the increase of the angle of attack to more than 6 degrees, the pitching moment curve became steeper, which means that the UAV had stronger longitudinal static stability at large angle of attack and also means that the UAV had good takeoff and landing characteristics and stall characteristics.

Through the analysis of aerodynamic data, it can be seen that the method of improving the UAV’s aerodynamic efficiency by increasing the reverse camber of airfoil and reducing the horizontal tail area was effective, which brought good aerodynamic efficiency.

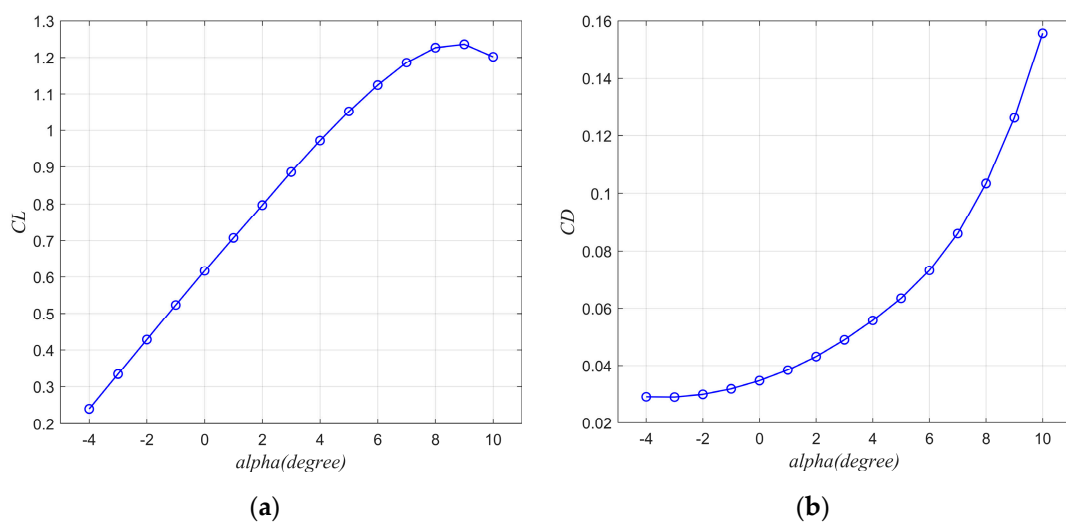


Figure 8. Cont.

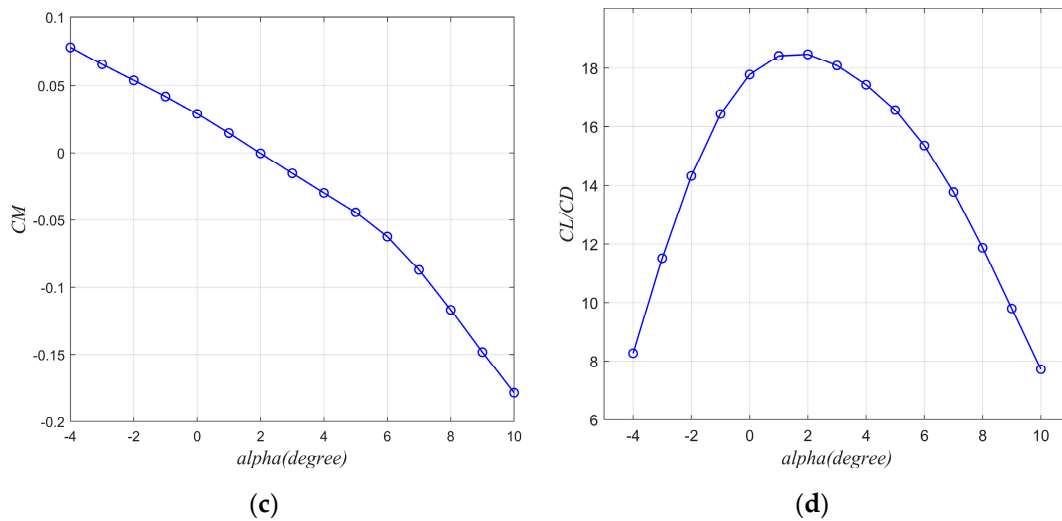


Figure 8. Computational Fluid Dynamics (CFD) result of cruise at 5000-m altitude of the UAV: (a) Lift coefficient, angle of attack data; (b) drag coefficient, angle of attack data; (c) pitching moment coefficient, angle of attack data; (d) lift–drag ratio data.

The mature conventional layout ensured the longitudinal stability of the UAV in the high angle of attack and adjacent stall state, which can meet the requirements of hand-launched takeoff and hard landing in the extreme environment without runway.

3.3. Structure and Avionics

The structure of MP Solar UAV was a traditional beam-rib structure made of carbon, KEVLAR, and balsa wood. The beam of the main wing was a rectangular hollow section beam consisting of rectangular carbon tubes arranged up and down and walls with lightening holes. The rectangular beam had better bending resistance than the circular carbon tube beam, which was harder to deform under overload caused by sudden wind, ensuring the safety of solar cells. The wing ribs, trusses, and the solar cells laid on the upper surface of the wing formed a shell structure, ensuring good torsional stiffness of the wing (Figure 9b).

To prevent the propeller from interfering with the optical payload, the fuselage was of a tail-pushed configuration, in which the propulsion system is located at the rear of the fuselage. The hard landing adopted by MP Solar UAV required the fuselage to have enough strength, so the fuselage structure (Figure 9a) adopted a shell structure composed of transverse mediastinum frame, truss, and skin.

The power generation and storage system consisted of solar cells, MPPT, and lithium-ion batteries, which were the core of the MP Solar UAV's perpetual flight. The energy was generated by 42 monocrystalline silicon solar cells laid on the surface of the main wing and stored in two high-energy density batteries located via MPPT. The packaged lithium-ion battery was connected in a 3S (11.1v) layout, which can provide 354 Wh energy. Solar cells had an energy conversion efficiency of about 23%.

It is important to note that low temperatures can seriously affect battery discharge performance and thus threaten flight endurance. Thus, the use of low thermal insulation material turned the fuselage into a closed cabin, and the self-heating from the batteries and avionics kept the cabin at the suitable temperature.

Avionics systems (See Figure 9a for avionics system arrangement) of MP Solar UAV included autopilot [14], digital radio, remote control (RC) receiver, sensors, propulsion systems, etc. In order to obtain necessary information of position velocity and altitude for flight controller, many low-cost and highly robust MEMS (micro-electro-mechanical systems) sensors were equipped on this UAV, including accelerometer gyroscope, magnetometer, barometer, and GPS. The actuation system was driven by two brushless servos to drive the rudder and all-moving elevator, which had high sensitivity and reliability. The propulsion system used a brushless motor direct drive 10- × 7-inch propeller, with

a maximum power output of about 430 W at takeoff. The UAV offered a fully manual mode to deal with a severe case of autopilot failure [15].

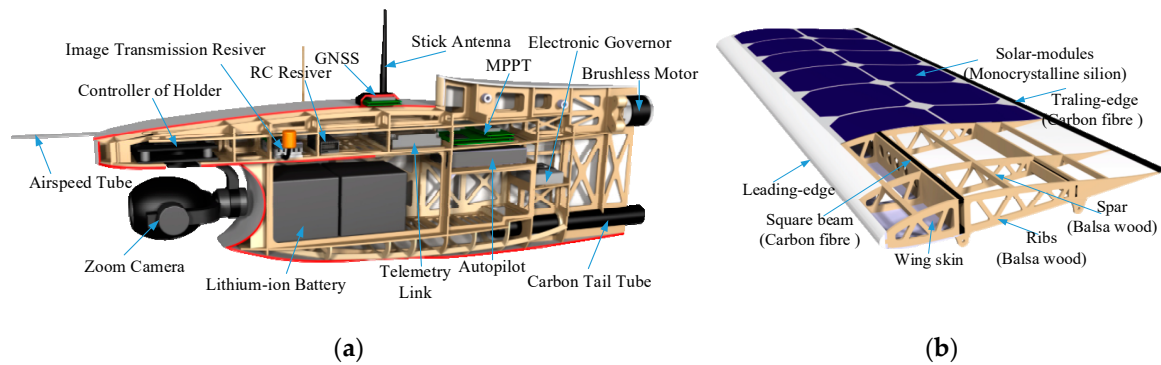


Figure 9. (a)The fuselage structure and arrangement of instruments, (b) wing structure.

MP Solar UAV was designed to have a maximum payload capacity of 450 g. Different functional payloads mean different payload weights, and the aircraft can be fitted with different loads to suit different missions. The aircraft had a designed payload capacity of 50 g for perpetual flight, which is enough to carry a small fixed-focus camera with video recording capability. The UAV can also carry a 450 g optical-infrared optoelectronic pod for complex missions at the expense of perpetual flight capability. The whole energy route of payload and avionics instruments are shown in Figure 10.

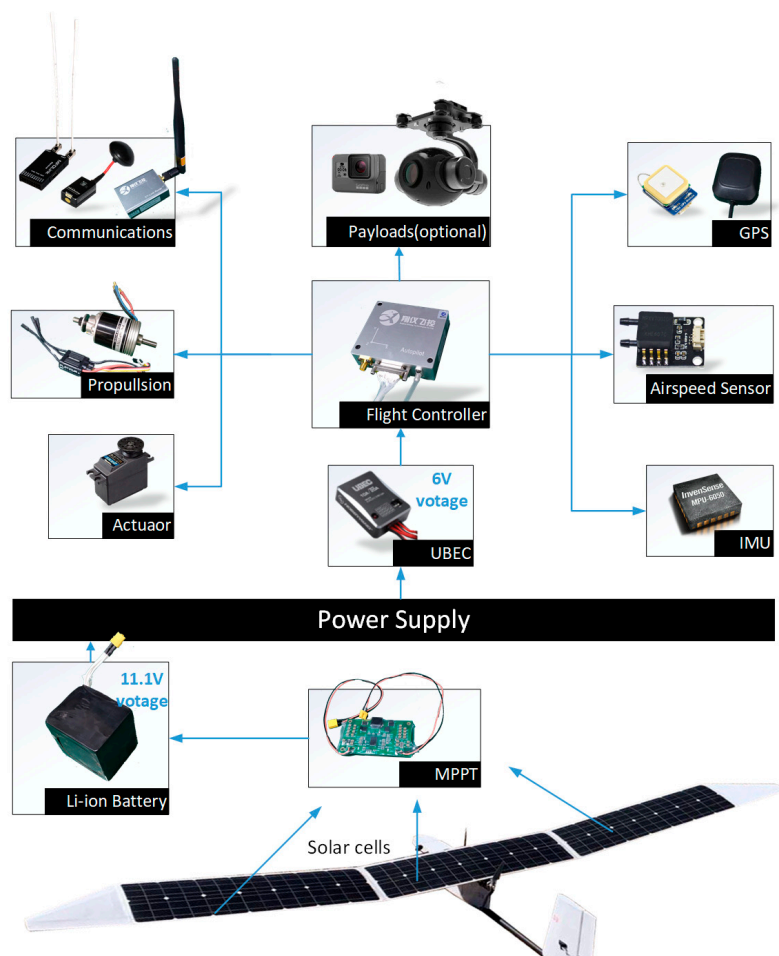


Figure 10. Topological system overview over the MP Solar UAV.

4. UAV Flight Control

4.1. Lateral-Directional Nonlinear Dynamic Model

The wings of a solar-powered UAV provide the main solar cell laying surface, so a complete wing without split by control surface is especially important for a small solar-powered UAV. In this paper, the MP Solar UAV was aileron-free and used rudder to control both yaw axis and roll axis. The rudder deflection generated yaw moment, and the sideslip angle generated by the rudder deflection also brought a large roll moment because the wing had a dihedral design [16]. The lateral-directional nonlinear dynamic model [17] of aileron-free UAV was established as Formula (19).

$$\begin{cases} \dot{v} = pw - ru + g \cos \theta \sin \varphi + Y/m \\ \dot{\varphi} = p + q \sin \varphi \tan \theta + r \cos \varphi \tan \theta \\ \dot{\psi} = q \sin \varphi \sec \theta + r \cos \varphi \sec \theta \\ \dot{p} = \Gamma_1 pq - \Gamma_2 qr + \Gamma_3 l + \Gamma_4 n \\ \dot{r} = \Gamma_5 pq - \Gamma_1 qr + \Gamma_4 l + \Gamma_6 n \end{cases} \tag{19}$$

where the specific expansion of symbols are shown in the Formula (20).

$$\begin{cases} \Gamma = I_x I_z - I_{xz}^2 \\ \Gamma_1 = I_{xz}(I_x - I_y + I_z)/\Gamma \\ \Gamma_2 = [I_z(I_z - I_y) + I_{xz}^2]/\Gamma \\ \Gamma_3 = I_z/\Gamma \\ \Gamma_4 = I_{xz}/\Gamma \\ \Gamma_5 = I_x(I_x - I_y) + I_{xz}^2 \\ \Gamma_6 = I_x/\Gamma \\ Y = \frac{\bar{q}bS}{2V}(C_{Yp}p + C_{Yr}r) + \bar{q}S(C_{Y\beta}\beta + C_{Y\delta_r}\delta_r) \\ l = \frac{\bar{q}b^2S}{2V}(C_{lp}p + C_{lr}r) + \bar{q}bS(C_{l\beta}\beta + C_{l\delta_r}\delta_r) \\ n = \frac{\bar{q}b^2S}{2V}(C_{np}p + C_{nr}r) + \bar{q}bS(C_{n\beta}\beta + C_{n\delta_r}\delta_r) \end{cases} \tag{20}$$

where $I_x, I_y, I_z,$ and I_{xz} are the moment of inertia and the product of inertia of the UAV, respectively. The $u, v,$ and w are the velocity component of flight path under the body axes. The $p, q,$ and r are the angular rate of the body axes. The $\varphi, \theta,$ and ψ are angle of roll, pitch, and yaw, respectively. Y, l, n are lateral force, rolling moment, and yawing moment. The \bar{q} is dynamic pressure and δ_r is the angle of rudder deflection.

4.2. Analysis of Stability and Flight Quality

By using Taylor expansion, the nonlinear dynamics model is linearized and the lateral-directional small-disturbance equations are obtained as Formula (21).

$$\dot{x} = Ax + Bu \tag{21}$$

where state vector $x = [\beta \ p \ r \ \varphi \ \psi]^T$, state matrix A is shown in Formula (22), and B is control matrix, control input $u = [\delta_r]^T$.

$$A = \begin{bmatrix} Y_\beta & \alpha^* + Y_p & Y_r - 1 & g \cos \theta^*/V^* & 0 \\ L_\beta & L_p & L_r & 0 & 0 \\ N_\beta & N_p & N_r & 0 & 0 \\ 0 & 1 & \tan \theta^* & 0 & 0 \\ 0 & 0 & \sec \theta^* & 0 & 0 \end{bmatrix} \tag{22}$$

where α^* and V^* represent angle of attack and speed of UAV at trim point. The characteristic roots of lateral-directional state matrix represent the flight quality of UAV lateral-directional mode.

The design mission environment of MP Solar UAV was for 4500-m elevation above plateau. Therefore, the aileron-free UAV still needs to have a good flight performance in high altitude. The change of the UAV's system characteristic roots with speed increase at an altitude of 500 m and 5000 m, respectively, are shown in Figure 11. The speed range was 8–12 m/s.

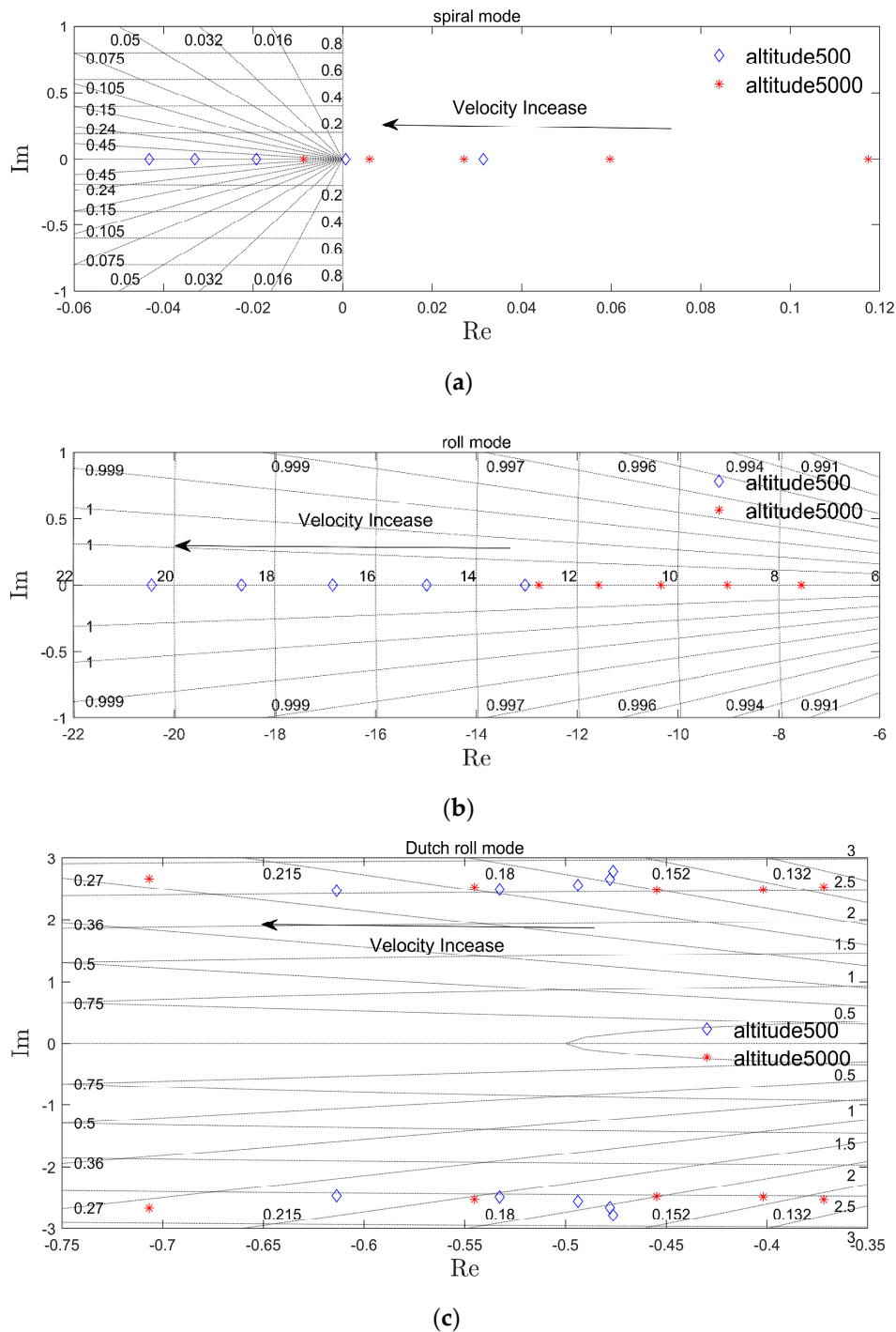


Figure 11. The change of system characteristic roots with different altitude and speed in lateral-directional mode. (a) Spiral mode. (b) Roll mode. (c) Dutch roll mode.

It can be seen from Figure 11a,b that, when flying at high altitude, the characteristic root of roll mode and spiral mode moved to the right of the complex plane compared with that at low altitude, and the flight quality became worse.

The move of characteristic roots of the Dutch roll mode (Figure 11c) in real axis had no obvious directionality, but the characteristic roots dispersion was larger than that of low-altitude flight, which means that the stability of the Dutch roll mode was more sensitive to the flight speed at high altitude. At the same altitude, with the increase of flight speed, the characteristic roots of lateral-directional mode all moved to the left of the complex plane, and the flight quality became better.

The Cooper–Harper rating is a systematic method of quantifying the results of an experiment, which is divided into three grades to describe the flight quality of an aircraft [18]. Among them, the level-one flight quality represents the flight quality to ensure the successful completion of all flight missions. At an altitude of 500 m, both the roll mode and the Dutch roll mode were of level-one flight quality in the full speed range. However, when the speed was lower than 9 m/s, the characteristic root of spiral mode was positive and the doubling time was 23 s. In other words, although the spiral mode diverged at a low speed, it still met the level-one flight quality requirements.

At an altitude of 5000 m, the maximum rolling constant of convergence time was 0.13. With the change of flight speed, the frequency of Dutch rolling mode almost remained unchanged, about 2.32, and the minimum damping was about 0.149. That is, both the rolling mode and Dutch rolling mode (Figure 11b,c) met the level-one quality within the full speed range of 5000 m. At the cruise speed of 10 m/s, the half-value period was 25.7 s, and the spiral mode met the level-one flight quality requirements. However, when the flight speed was lower than 9 m/s, the spiral mode no longer met the level-one flight quality, and continued to deteriorate with the flight speed decrease. Therefore, high-altitude flight needs to avoid flying at too low a speed to prevent deterioration of flight quality.

4.3. Analysis of Lateral-Directional Maneuverability

The UAVs with conventional configuration use aileron and rudder to control roll and sideslip, while MP Solar UAV with aileron-free design uses rudder to controls both roll and sideslip. Therefore, it is necessary to analyze the maneuvering characteristics of aileron-free UAV [19]. Figure 12 shows the free response of rudder deflection during cruise at altitudes of 500 m and 5000 m.

According to Figure 12, the rudder deflection of the UAV can cause both sideslip angle and roll angle, scilicet, and the rudder can be used for rolling and yaw control. There was an obvious phase difference between the roll angular rate and the sideslip angle, which indicates that the roll angle of the UAV was mainly caused by the sideslip angle, rather than the rudder deflection. Compared with aileron control roll, rudder control is an indirect process with slower response, which needs to be considered when designing the control laws.

Compared with the flight at low altitude, the response frequency of the UAV at high altitude was almost the same, but the amplitude was larger, which is consistent with the result in the Figure 11 that the system damping decreased as the altitude increased. After the convergence of shock, the effect of rudder control sideslip at different altitudes was basically the same, while the effect of high-altitude control was better than that of low-altitude control.

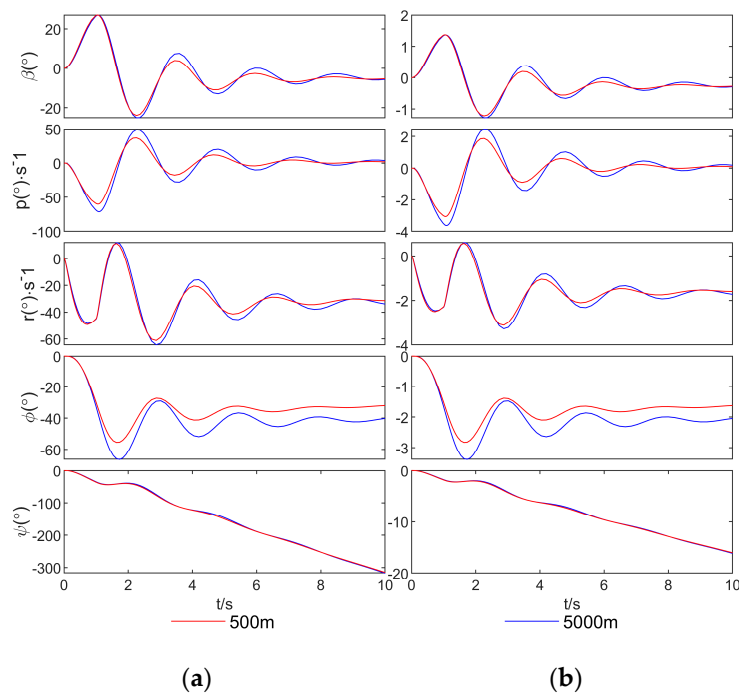


Figure 12. Free response of rudder deflection at low altitude and high altitude: (a) Rudder deflect 20 degree. (b) rudder deflect 1 degree.

4.4. Successive Loop Closure Flight Control

4.4.1. Longitudinal Control Law

The mission environment of MP Solar UAV was cruising at a speed of 10 m/s on a plateau at an altitude of 4500 m. The longitudinal control input of the UAV was all-moving elevator and throttle, and the longitudinal dynamic state space, which is shown in Formula (23), was extended to consider the influence of elevator and throttle.

$$\begin{aligned} \dot{\mathbf{x}}_{lon} &= \mathbf{A}_{lon}\mathbf{x}_{lon} + \mathbf{B}_{lon}\mathbf{u}_{lon} \\ \mathbf{x}_{lon} &= \begin{bmatrix} u & w & q & \theta \end{bmatrix}^T \end{aligned} \tag{23}$$

Where u , w , q , and θ correspond to x -, z - axis velocity component, pitch angular rate, and pitch angle. The control law of longitudinal inner loop was altitude hold (Formula (24)), and the output was command signal of deflection angle of all-moving elevator and throttle.

$$\begin{aligned} q_c &= k_q(\theta_c - \theta) \\ \delta_e &= (k_p + k_{p_i} \cdot \frac{1}{s} + k_{p_d} \cdot s)(q_c - q) \end{aligned} \tag{24}$$

The outer loop was the height and airspeed hold control law, which are shown in Formula (25), and the simulation results of the UAV's pitch angle and altitude command tracking are shown in the Figure 13. Both the pitch angle and the altitude can well realize the command tracking without static error or overshoot, and the response time of the pitch angle command was about 1.1 s.

$$\begin{aligned} \theta^c &= k_{p_h}(h^c - h) + \frac{k_{i_h}}{s}(h^c - h) \\ \delta_t &= k_{p_v}(V_a^c - V_a) + \frac{k_{i_v}}{s}(V_a^c - V_a) \end{aligned} \tag{25}$$

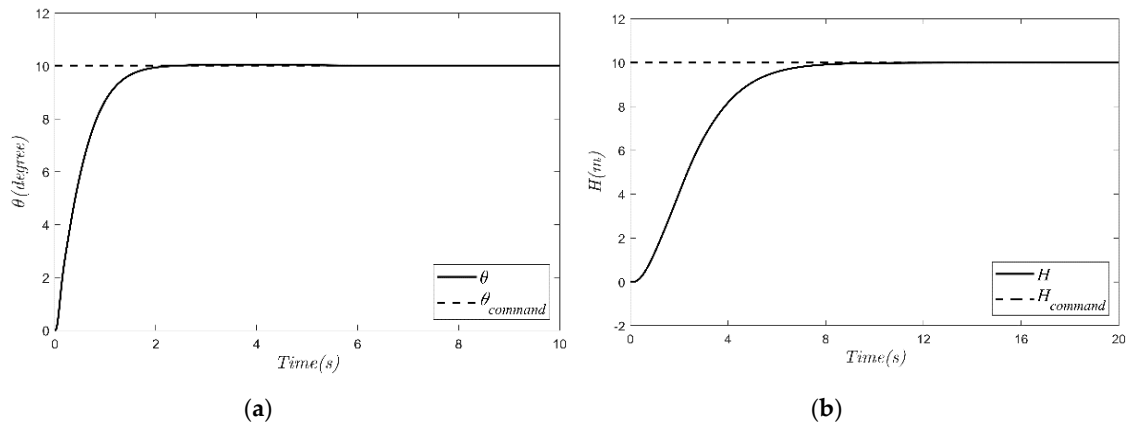


Figure 13. Simulation of pitch angle and altitude command tracking: (a) Pitch angle tracking. (b) Altitude tracking.

4.4.2. Lateral-Directional Control Law

The lateral-directional control law is still based on the successive closed-loop theory [20]. For the UAV with aileron-free design, the rudder was the only input for lateral-directional control. That is, the rudder can simultaneously control the two channels of roll and sideslip: Channel 1, the rudder was treated as a pseudo-aileron, controlling the roll channel. Formula (26) is the control law when the rudder is used as a pseudo-aileron. Channel 2, the rudder was used to control the sideslip of the UAV, and Formula (27) is the output of rudder command during coordinated turn.

$$\begin{aligned} p_c &= (k_{p_\phi} + k_{d_\phi} \cdot s)(\phi_c - \phi) \\ \delta_a &= (k_p + k_{p_d} \cdot s)(p_c - p) \end{aligned} \tag{26}$$

$$\begin{aligned} r_c &= \frac{g}{V_0} \tan \phi_c \\ \delta_r &= k_r(r_c - r) \end{aligned} \tag{27}$$

The outer loop was a straight-line trajectory tracking by the L_1 method [21], Figure 14 shows the path diagram of UAV and linear target. In the figure, d is track error, L_1 is the distance between conference point and UAV, V is velocity component of the horizontal plane, χ is the flight path angle, as is expected lateral acceleration, and ψ_t is the azimuth angle of target trajectory. The control instruction of horizontal trajectory tracking based on L_1 method is shown in Formula (28).

$$\begin{aligned} a_s &= 2 \frac{V^2}{L_1} \sin \eta \approx 2 \frac{V}{L_1} \left(\dot{d} + \frac{V}{L_1} d \right) \\ \phi_{cmd} &= \arctan \left(2 \frac{V}{L_1 g} \left(\dot{d} + \frac{V}{L_1} d \right) \right) \\ \psi_{cmd} &= \psi_t + \eta_1 \end{aligned} \tag{28}$$

The simulation results of UAV straight-line trajectory tracking are shown in the Figure 15. Figure 15a shows that the response time of the roll angle command was about 1.4s and there was no static error or overshoot. Figure 15b shows that the response time of lateral distance command (50 m) was about 10.39 s with 2.12 m overshoot. The simulation results show that the trajectory tracking control based on L_1 method is feasible for the UAV flight at 4500-m altitude with aileron-free configuration.

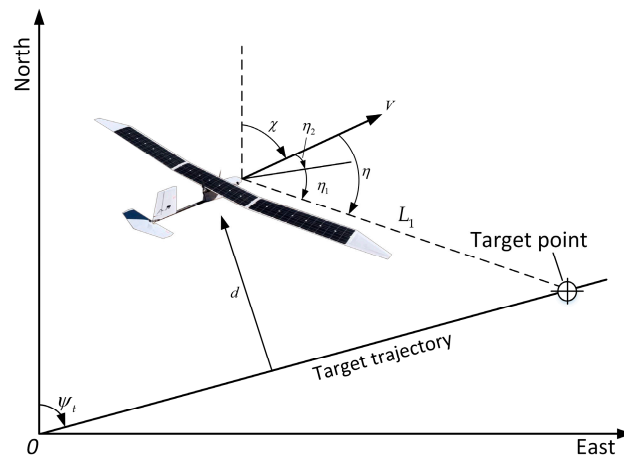


Figure 14. Schematic diagram of UAV and desired flight path.

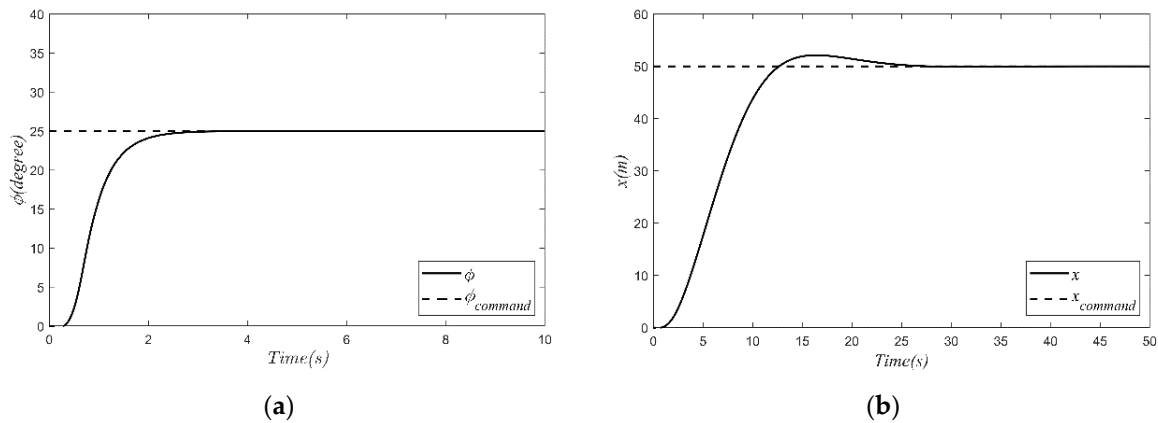


Figure 15. Simulation of straight-line trajectory tracking: (a) Roll angle command tracking, (b) lateral distance command tracking.

5. Field Experiment

5.1. Experiment Environment

The target mission area of the MP Solar UAV was Qiangtang and Hoh Xil in Tibet (low temperature and high altitude), where it is harsh for human activities. The purpose of the experiment was to verify whether the scheme had the ability to fly in extreme environments and to analyze the feasibility of perpetual flight in the plateau region.

Full-system flight tests of MP Solar UAV were performed in extreme environments, as shown in the Figure 16. The experiment site is located at 4604 m in Qiangtang, (31.988° E, 87.317° N) and the experiment was conducted in winter with a temperature of $-30\text{ }^{\circ}\text{C}$. Vehicle-mounted takeoff was adopted because the human body could not withstand strenuous activity at high altitude. The whole process of flight experiments included hand-launched takeoff in a car, autonomous climb, cruise, and slide [22].

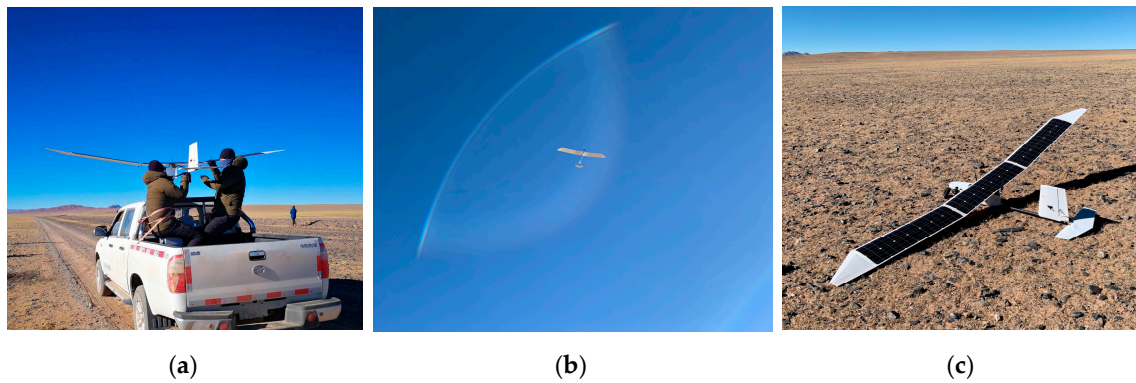


Figure 16. The high-altitude field experiment of UAV in Qiangtang, Tibet: (a) Vehicle-mounted takeoff, (b) cruise phase for mission, (c) hard landing in extreme environment.

5.2. Flight Parameters of HighAltitude Experiment

The flight parameters of takeoff and cruise at high altitude are shown in Figure 17. Figure 17a shows the climbing process of the UAV: The UAV took off from an altitude of 4600 m, climbed to 4700 m, and turned to level flight. In order to ensure the safety of taking off at high altitude, the vehicle-mounted takeoff was adopted, and the instantaneous airspeed of departure was 16 m/s. Figure 17b presents a part of parameters from the stable cruise phase. The absolute cruising altitude of the UAV was 4700 m, the altitude was about 100 m, cruise airspeed was about 10.5 m/s, and the flight trajectory was a circular route around the mission area.

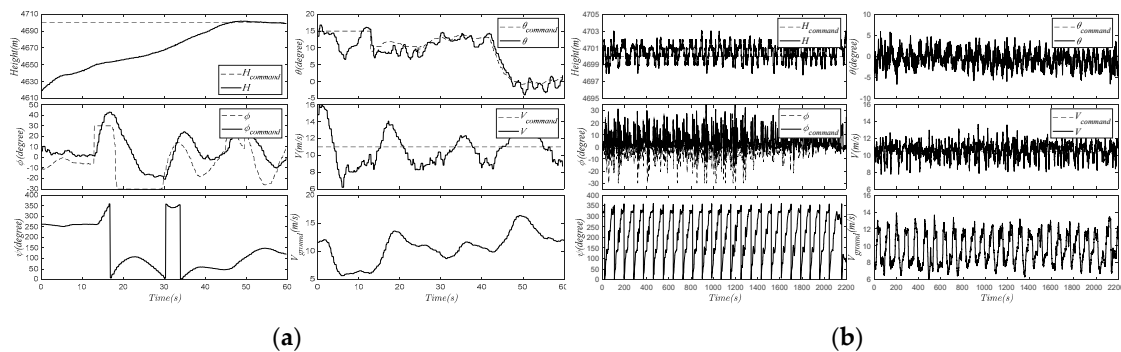


Figure 17. Flight result of field experiment: (a) Climb phase, (b) cruise phase.

In this field experiment, the UAV’s mission flight path mainly included a quadrilateral flight path and a circular flight path. The quadrilateral flight path was suitable for takeoff and landing and searching targets in a wide range. The circular flight path was used for tracking and monitoring designated areas or targets. Figure 18 shows the circular flight path and the quadrilateral flight path in the flight test, respectively.

From the circular flight path (Figure 18a), it can be seen that the aileron-free UAV tracked the path well under the condition of no wind, and the flight trajectory had almost no overshoot. Figure 18b shows the situation of the UAV tracking a quadrilateral flight path with 7 m/s positive wind. The UAV tracked the path well on the upwind side. However, on the downwind side, the flight path had overshoot. In general, the aileron-free UAV achieved the required path tracking for the mission, although maybe the tracking was less accurate than aileron UAV in windy conditions.

In order to increase the proportion of solar cells laid and reduce the structural weight of the wings brought by the control surface, the UAV eliminated ailerons as roll control and used a rudder to control both roll axis and yaw axis. Figure 12 shows the free response simulation of rudder deflection when the UAV flew at different altitudes. In the flight test, the control characteristics of the UAV were verified.

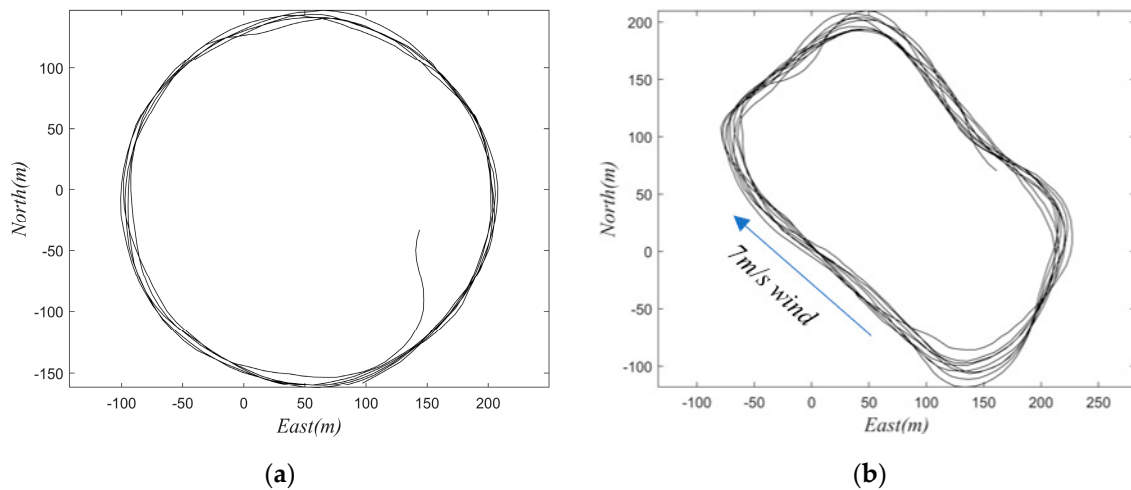


Figure 18. The flight path of the solar-powered UAV: (a) Circular flight path without wind, (b) quadrilateral flight path with 7 m/s wind.

Figure 19 shows the data of the roll angle and rudder deflection when the UAV changed from a circular flight path to a straight-line flight path, which means the UAV turned left from the clockwise circular route and entered a straight-line flight path. As seen in the figure, the roll angle command appeared at 15 s with a command value of 30 degrees, and the rudder deflected after 0.3 s and a deflection value of 28 degrees after 1.5 s. The roll angle response time was slightly slower, about 5 s, because the roll angle of the aileron-free UAV was not directly caused by the rudder deflection but by the sideslip, which was an indirect process for the rudder. In general, the response characteristics of the roll angle were consistent with the simulation results.

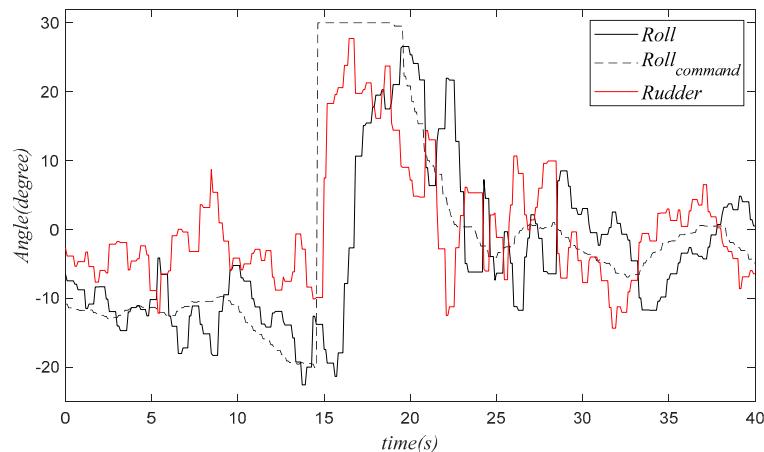
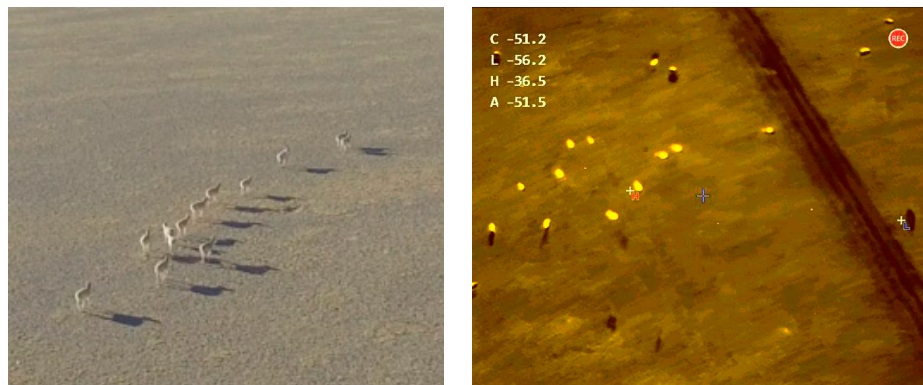


Figure 19. Rudder—roll angle response.

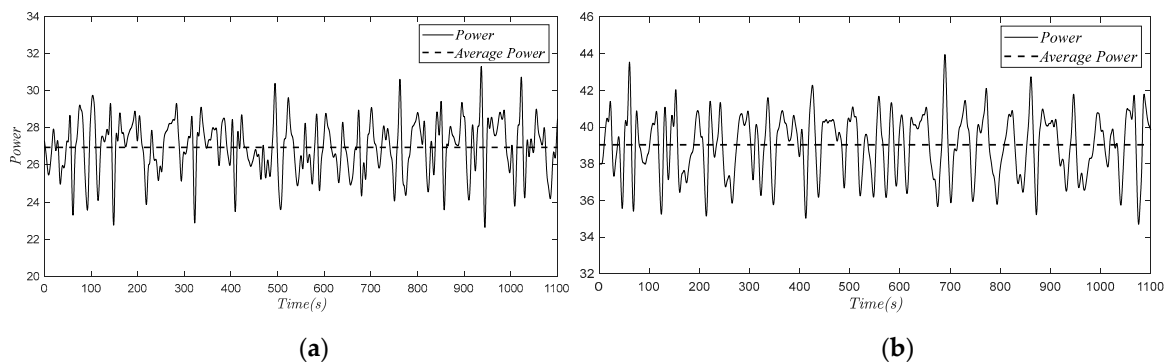
According to different mission objectives, the UAV can carry different weight and power consumption of the payloads. Weight and power consumption and other parameters will affect the weight coefficient of batteries. Heavier and higher power consumption of payload usually means worse flight endurance. In the field test, the UAV completed its flight test with two different payloads: Payload 1 was a small fixed-focus camera weighing only 50 g and a low-power transmission with power of 600 mW and payload 2 was an optical-infrared composite optronics pod weighting 450 g and a remote digital graph transmission with an effective distance of 15 km and a power of 15 W. In the case of constant total weight, different payloads not only mean different additional power consumption, but also affect the carrying capacity of batteries, which is closely related to flight endurance. Figure 20 shows different payloads applied to endangered animal monitoring.



(a) (b)

Figure 20. Different payloads for endangered animals: (a) Optical image, (b) infrared image.

The Figure 21 shows the cruising power of the UAV with two different payloads. The dotted line in the figure is the average cruising power, which can be used to estimate the aircraft’s battery endurance to determine whether the UAV is capable of flying across the night, which is a prerequisite of perpetual flight.



(a) (b)

Figure 21. Cruise power data of the UAV with different payload configurations at altitude of 4700 m: (a) Small fixed-focus camera with low-power transmission, (b) optical-infrared combined optoelectronic pod with remote digital transmission.

Different seasons have different hours of sunshine, which is closely related to the flight endurance. As can be seen from the Figure 21a, the cruising power of the UAV with payload 1 was about 27 W, which means the battery endurance of the UAV was 13.3 h, which was enough to allow the UAV to cross the night (perpetual flight) in summer. In summer (take July 1 as an example), the flight time that the solar cell power can meet the cruise consumption is about 11.7 h, and the night time is 12.3 h to simplify the neglect of transition time. In winter (take December 10 as an example), the maximum solar irradiance and sunshine duration are shorter, and considering the influence of low temperature in winter on battery discharge efficiency, the flight endurance that the solar cell power can meet the cruise consumption is only 6.1 h, which means the UAV cannot cross the night. If the UAV takes off at midnight, it reaches its energy balance point when batteries run out and the UAV will gain its maximum endurance of 29.7 h.

As can be seen from the Figure 21b, the cruising power of the UAV with payload 1 was about 39 W, which means the battery endurance of the UAV was 9.2 h and the UAV cannot cross the night with payload 2. The maximum endurance in summer and winter are 29.3 h and 20.8 h, respectively.

On the whole, at an altitude of 4600 m, the MP Solar UAV can achieve autonomous climb, cruise, hover, and descent control, completing the feasibility verification of the whole process of control system

design. The cruise power data of the UAV with different loads indicate that it is feasible for the UAV to achieve perpetual flight at an altitude of 4600 m, which verifies the correctness of the design method.

The permanent flight of solar UAV requires both seasons and mission loads. Less ideal seasons and more stringent mission requirements will prevent the UAV from achieving perpetual flight, but it still has better endurance, which is the unique advantage of solar-powered UAV.

6. Conclusions

This paper proposed a complete research process of a hand-launched solar-powered UAV for plateau, from conceptual design method, detailed design, dynamics modeling, control scheme design, numerical simulation, and hardware in the loop simulation experiment to field experiments.

In order to achieve perpetual flight in the plateau region, this paper proposed a conceptual design method of solar-powered UAV based on energy balance and the optimal parameter solution was found for the plateau region as the mission environment. The main conceptual parameters indicate that it is feasible for small, solar-powered UAV to fly day and night (perpetual flight) at high altitudes during the summer. In the design model, the solar irradiance model took latitude, altitude, date, and other parameters as input, which can more accurately reflect the sunshine conditions at different geographical locations and time compared with the simplified model. In this paper, real irradiance data were collected by the total irradiance meter to modify the model and the main parameters of the modified model, such as maximum illumination and sunshine duration, were in good agreement with the experimental data.

In view of the low-temperature flight environment of the UAV, the temperature influence factor was introduced into the traditional battery model, and the battery weight model considering the low-temperature influence was proposed. Among them, the temperature influence factor was measured by the low-temperature discharge test of the battery.

To validate the design methodology, a full-system, hand-launched, solar-powered UAV was designed and fabricated, including configuration, structure, payload selection, and whole avionics.

Based on the six-degrees-of-freedom equation of motion, this paper analyzed the changes in the stability and maneuverability of aileron-free UAV at high altitude. At high altitude, the stability of both spiral mode and roll mode were worse, and the speed sensitivity of Dutch roll mode increased. At high altitude, the damping of UAV was reduced and the oscillation convergence after disturbance was slower. According to the flight conditions of the plateau, the longitudinal height tracking control law with continuous closed loop and the lateral-directional trajectory tracking control law based on L_1 method were designed, respectively.

Finally, the flight test was conducted at an altitude of 4600 m in Qiangtang (31.988° E, 87.317° N), Tibet, and the feasibility of the design method and control system was verified. The cruise power data of the UAV with different loads indicate that it is feasible for the UAV to achieve perpetual flight at an altitude of 4600 m during summer. Less ideal seasons and more stringent mission requirements will prevent the UAV from achieving perpetual flight, but it still has better endurance, which is the unique advantage of solar-powered UAV. The design method and verification method can be extended to other similar UAV platform.

Author Contributions: X.Z. (Xin Zhao) and Z.Z. conducted the whole design method and system modeling. X.Z. (Xin Zhao) and A.G. contributed the designing and manufacture of hardware system of prototype. X.Z. (Xiaoping Zhu) analyzed the experiment result. X.Z. (Xin Zhao) and Z.Z. wrote the paper. All authors have read and agreed to the published version of the manuscript.

Funding: This research was funded by the Innovation plan of the Institute grant number TC2018DYDS24 and Key R&D Projects in Shaanxi Province of China grant number 2018ZDCXL-GY-03-04.

Conflicts of Interest: The authors declare no conflict of interest.

References

1. Colella, N.; Wenneker, G. Pathfinder: Developing a solar rechargeable aircraft. *IEEE Potentials* **1996**, *15*, 18–23. [[CrossRef](#)]
2. Helios Prototype Solar-Powered Aircraft. Available online: <https://www.nasa.gov/centers/dryden/history/pastprojects/Helios/index.html> (accessed on 20 December 2019).
3. Solar Impulse 2 Detailed Route. Available online: <https://zh.m.wikipedia.org/zh-cn/SolarImpulse2> (accessed on 6 January 2020).
4. Ackerman, E. Giant Solar-Powered UAVs are Atmospheric Satellites. Available online: <https://spectrum.ieee.org/automaton/robotics/drones/giant-solar-powered-uavs-are-atmospheric-satellites> (accessed on 6 January 2020).
5. QinetiQ. QinetiQ files for three world records for its Zephyr Solar powered UAV. *Asia-Pac. Def. Rep.* **2010**, *36*, 8.
6. Airbus Zephyr S Breaks World Flight Endurance Record during Maiden Flight. Available online: <https://www.sae.org/news/2018/08/airbus-zephyr-s-breaks-world-flight-endurance-record-during-maiden-flight> (accessed on 6 January 2020).
7. Noth, A. Design of Solar Powered Airplanes for Continuous Flight. Ph.D. Thesis, Swiss Federal Institute of Technology (ETH), Zürich, Switzerland, September 2008.
8. Oettershagen, P.; Stastny, T.; Hinzmann, T. Robotic technologies for solar-powered UAVs: Fully autonomous updraft-aware aerial sensing for multiday search-and-rescue missions. *J. Field Robot.* **2017**, *35*, 1–29. [[CrossRef](#)]
9. Keidel, B. Auslegung und Simulation von Hochfliegenden Dauerhaft Stationierbaren Solardrohnen. Ph.D. Thesis, Technischen Universität München, München, Germany, 2000.
10. Badescu, V.; Gueymard, C.A.; Cheval, S.; Oprea, C.; Baciu, M.; Dumitrescu, A.; Iacobescu, F.; Milos, I.; Rada, C. Computing global and diffuse solar hourly irradiation on clear sky. Review and testing of 54 models. *J. Renew. Sustain. Energy Rev.* **2012**, *16*, 1636–1656. [[CrossRef](#)]
11. Romeo, G.; Frulla, G.; Cestino, E.; Corsino, G. Heliplat: Design, Aerodynamic, Structural Analysis of Long-Endurance Solar-Powered Stratospheric Platform. *J. J. Aircr.* **2004**, *41*, 1505–1520. [[CrossRef](#)]
12. Youngblood, J.W.; Talay, T.A.; Pegg, R.J. Design of Long-Endurance Unmanned Airplanes Incorporating Solar and Fuel Cell Propulsion. In Proceedings of the The 20th Joint Propulsion Conference, AIAA-84-1430, Cincinnati, OH, USA, 11–13 June 1984.
13. Rizzo, E.; Frediani, A. A Model for Solar Powered Aircraft Preliminary Design. In Proceedings of the International Conference on Computational & Experimental Engineering & Sciences 04, Madeira, Portugal, 26–29 July 2004; Volume 1, pp. 39–54.
14. Ebeid, E.; Skriver, M.; Terkildsen, K.H.; Jensen, K.; Schultz, U.P. A Survey of Open-Source UAV Flight Controllers and Flight Simulators. *Microprocess. Microsyst.* **2018**, *61*, 11–20. [[CrossRef](#)]
15. Arifianto, O.; Farhood, M. Development and Modeling of a Low-Cost Unmanned Aerial Vehicle Research Platform. *J. Intell. Robot. Syst.* **2015**, *80*, 139–164. [[CrossRef](#)]
16. Cheng, X.; Wang, H.P.; Zhang, Y.Z. Electric and no aileron SUAV's lateral-direct dynamic characters. *Flight Dyn.* **2009**, *27*, 74–77. (In Chinese)
17. Beard, R.W.; Mclain, T.W. *Small Unmanned Aircraft: Theory and Practice*; Princeton University Press: Princeton, NJ, USA, 2012; pp. 52–92.
18. Bandu, N.P. *Performance, Stability, Dynamics, and Control of Airplanes*; American Institute of Aeronautics and Astronautics: Reston, VA, USA, 2013; pp. 511–514. (In Chinese)
19. Ma, Z.Y.; Zhu, X.P.; Zhou, Z. A lateral-directional control method combining rudder and propeller for full-wing solar-powered UAV. *J. Acta Aeronaut. Et Astronaut. Sin.* **2018**, *39*, 321633. (In Chinese)
20. Ma, Z.Y.; Zhu, X.P.; Zhou, Z. On-ground lateral direction control for an unswept fly-wing UAV. *Aeronaut. J.* **2019**, *123*, 416–432. [[CrossRef](#)]

21. Park, S.; Deyst, J.; How, J.P. A new nonlinear guidance logic for trajectory tracking. In Proceedings of the AIAA Guidance, Navigation, and Control Conference an Exhibit, Reston, VA, USA, 16–19 August 2004.
22. Guo, A.; Zhou, Z.; Zhu, X.; Bai, F. Low-Cost Sensors State Estimation Algorithm for a Small Hand-Launched Solar-Powered UAV. *Sensors* **2019**, *19*, 4627. [[CrossRef](#)] [[PubMed](#)]



© 2020 by the authors. Licensee MDPI, Basel, Switzerland. This article is an open access article distributed under the terms and conditions of the Creative Commons Attribution (CC BY) license (<http://creativecommons.org/licenses/by/4.0/>).